A study of the F-giant star θ Scorpii A: a post-merger rapid rotator?

Fiona Lewis,[1]★ Jeremy Bailey [●],[1]★ Daniel V. Cotton [●],[2,3,4,5] Ian D. Howarth [●],[6]
Lucyna Kedziora-Chudczer [●][5] and Floor van Leeuwen[7]

[1]*School of Physics, University of New South Wales, Sydney, NSW 2052, Australia*
[2]*Monterey Institute for Research in Astronomy, 200 Eighth Street, Marina, CA 93933, USA*
[3]*Anglo Australian Telescope, Australian National University, 418 Observatory Road, Coonabarabran, NSW 2357, Australia*
[4]*Western Sydney University, Locked Bag 1797, Penrith-South DC, NSW 1797, Australia*
[5]*Centre for Astrophysics, University of Southern Queensland, Toowoomba, QLD 4350, Australia*
[6]*Department of Physics and Astronomy, University College London, Gower Street, London WC1E 6BT, UK*
[7]*Institute of Astronomy, University of Cambridge, Madingley Road, Cambridge CB3 0HA, UK*

ABSTRACT

We report high-precision observations of the linear polarization of the F1III star θ Scorpii. The polarization has a wavelength dependence of the form expected for a rapid rotator, but with an amplitude several times larger than seen in otherwise similar main-sequence stars. This confirms the expectation that lower-gravity stars should have stronger rotational-polarization signatures as a consequence of the density dependence of the ratio of scattering to absorption opacities. By modelling the polarization, together with additional observational constraints (incorporating a revised analysis of *Hipparcos* astrometry, which clarifies the system's binary status), we determine a set of precise stellar parameters, including a rotation rate $\omega \, (= \Omega / \Omega_c) \geq 0.94$, polar gravity $\log(g_p) = 2.091^{+0.042}_{-0.039}$ (dex cgs), mass $3.10^{+0.37}_{-0.32}$ M$_\odot$, and luminosity $\log(L/L_\odot) = 3.149^{+0.041}_{-0.028}$. These values are incompatible with evolutionary models of single rotating stars, with the star rotating too rapidly for its evolutionary stage, and being undermassive for its luminosity. We conclude that θ Sco A is most probably the product of a binary merger.

Key words: polarization – techniques: polarimetric – binaries: close – stars: evolution – stars: rotation.

1 INTRODUCTION

Intrinsic stellar polarization was first predicted by Chandrasekhar (1946). He determined that, for a pure electron-scattering atmosphere, the radiation emerging from the stellar limb should be substantially linearly polarized. For a spherical star this polarization will average to zero, but a net polarization should result if there is a departure from spherical symmetry. Harrington & Collins (1968) suggested that the distortion of a star due to rapid rotation could result in observable polarization, although calculations with more realistic non-grey stellar-atmosphere models, taking into account both scattering and absorption (Code 1950; Collins 1970; Sonneborn 1982), led to predictions of lower polarization levels at visible wavelengths. Consequently, it is only as a result of recent advances in instrumentation that the polarization due to rotational distortion has been detected, first in the B7 V star Regulus (Cotton et al. 2017a) and subsequently in the A5 IV star α Oph (Bailey et al. 2020b).

The polarization produced by rotational distortion is identifiable through its distinctive wavelength dependence. In hotter stars, such as Regulus (Cotton et al. 2017a), the polarization shows a reversal of sign in the optical, being parallel to the star's rotation axis at red wavelengths but perpendicular in the blue. In cooler stars, such as α Oph, the optical polarization is always perpendicular to the rotation axis, but falls from a relatively high value around ∼400 nm to near zero at wavelengths of ∼800 nm and longer.

The polarization produced by scattering in stellar atmospheres is predicted to be strongly dependent on gravity (e.g. fig. 2 and supplementary fig. 4 in Cotton et al. 2017a). This is because the mass opacity due to scattering processes is independent of density, while the opacity due to most continuum absorption processes is roughly proportional to density (Kramers 1923). A lower density (as found in lower gravity stars) therefore results in an increased importance of scattering relative to absorption, and hence in higher levels of polarization. This applies to stellar polarization due to rotational distortion (Cotton et al. 2017a; Bailey et al. 2020b), to photospheric 'reflection' in binary systems (Bailey et al. 2019; Cotton et al. 2020), and to non-radial pulsation (Cotton et al. 2022). In all these cases, giant stars should show higher polarization than main-sequence stars if other factors are equivalent.

In this paper, we test that prediction for the case of stellar rotation. Our target, θ Scorpii (Sargas, HD 159532), was selected as a bright, rapid rotator ($V = 1.87$; Johnson et al. 1966), classified as F1III by Gray & Garrison (1989). van Belle (2012) included it in a list of candidates for investigation with optical interferometry, and a detailed interferometric study of the star is reported by Domiciano de Souza et al. (2018).
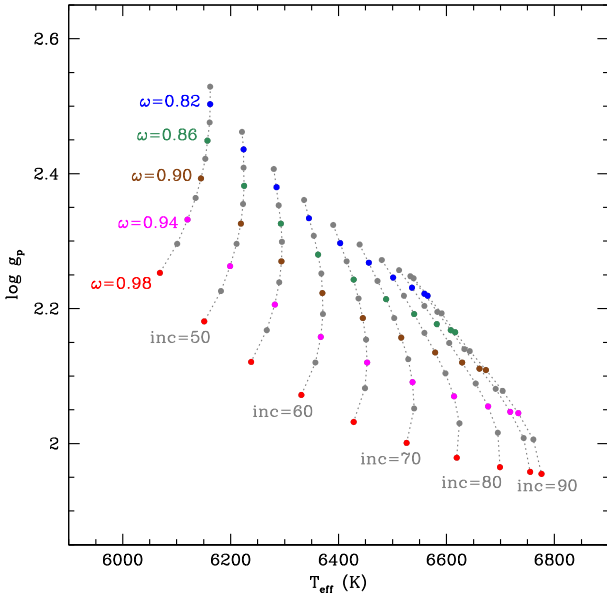
2 OBSERVATIONS

Between 2014 March and 2018 August, we obtained 13 high-precision polarimetric observations of θ Sco in seven photometric passbands, using HIPPI (the HIgh Precision Polarimetric Instrument; Bailey et al. 2015) and its successor HIPPI-2 (Bailey et al. 2020a)

★ E-mail: lewis.fiona@gmail.com (FL); j.bailey@unsw.edu.au (JB)
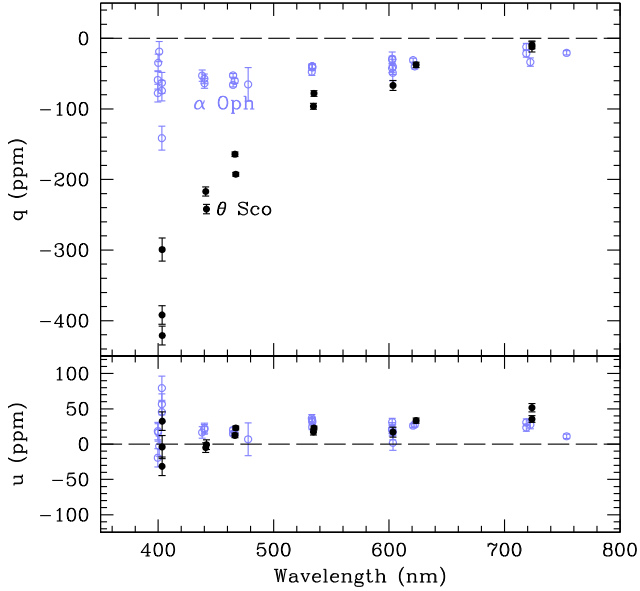
Figure 1. Polarization observations of θ Sco (black dots). The strong wavelength dependence seen in the q Stokes parameter is of the form expected for rapid rotation. For comparison we plot, as blue circles, the polarization data on the rapidly rotating main-sequence star α Oph (Bailey et al. 2020b). Much higher polarization levels are seen in θ Sco. The α Oph data have been rotated to put the polarization into the negative q parameter as it is in θ Sco.

Figure 2. Temperature–gravity tracks for values of ω and i for which the models discussed in Section 4.2 reproduce the shape and level of the observed flux distribution, and $v_e \sin i$.

on the 3.9-m Anglo-Australian Telescope (AAT) at Siding Spring Observatory. Standard operating procedures for these instruments were followed, with the data reduced using procedures described (for HIPPI-2) by Bailey et al. (2020a).

Originally developed for sensitive exoplanet work of the kind most recently reported by Bailey et al. (2021), both instruments used Ferro-electric Liquid Crystal (FLC) modulators to achieve the rapid, 500 Hz, modulation required for high precision. Observations were
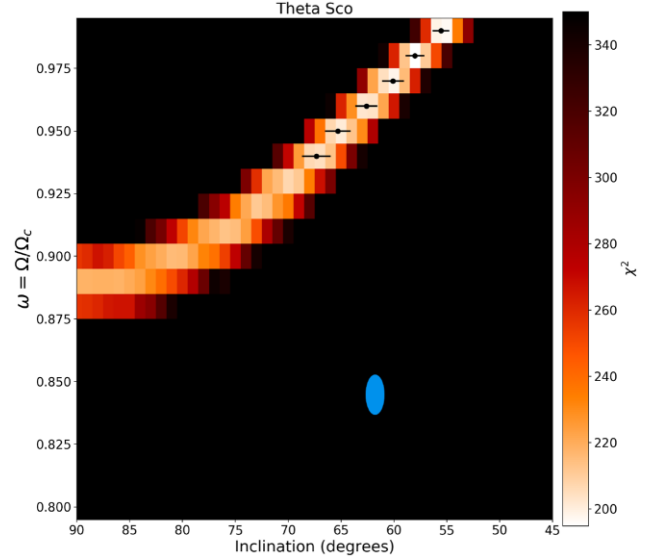
Figure 3. Results of the χ^2 analysis of the polarization of θ Sco. The colour bar indicates the χ^2 value (with lower χ^2 indicating a closer fit of models and data). As described in Section 4.2, the parameter set for each cell in this grid represents a model star that matches the observed spectrum; the χ^2 values show how well (or badly) each of these models also fits the observed polarization. Error bars on points in the best-fitting 'valley' are the result of bootstrap analyses for specific ω values (Section 5.2). The blue dot indicates the solution obtained by Domiciano de Souza et al. (2018; cf. Section 5.4); dot size approximately matches the 1σ error bars they quote.

made using either blue-sensitive Hamamatsu H10720-210 or red-sensitive Hamamatsu H10720-20 photo-multiplier tubes (PMTs) as the detectors.

For the HIPPI-2 observations, our standard filter set, described in Bailey et al. (2020a), was used; briefly, this includes 425- and 500-nm short-pass filters (425SP, 500SP), SDSS g', Johnson V, SDSS r' and a 650 nm long-pass (650LP) filter. The one HIPPI observation used an Omega Optics version of the SDSS g' filter instead of the Astrodon versions used with HIPPI-2. The blue-sensitive PMTs were paired with most of the filters, with the red-sensitive PMTs used for the 650LP observations, and for one of the r' observations.

The small amount of polarization arising in the telescope optics results in zero-point offsets in our observations. These are corrected for by reference to the straight mean of several observations of low-polarization standard stars, details of which are given in Bailey et al. (2020a). Similarly, the position angle (θ, measured eastward from celestial north) is calibrated by reference to literature measurements of high-polarization standards, also given in Bailey et al. (2020a). A summary of the calibrations and each observing run is given in Table 1.

Our observations of θ Sco are summarized in Table 2; here the instrumental positioning error, resulting from inhomogeneities across the face of the FLC, is included in the reported uncertainties. The data are presented in order of effective wavelength, and are plotted in Fig. 1. The strong wavelength dependence seen in the normalized Stokes parameter q ($=Q/I$) has the form expected for polarization resulting from rapid rotation, and the effect is much larger than seen in the rapidly rotating main-sequence star α Oph (Bailey et al. 2020b).

While the wavelength dependence is clearly seen in Fig. 1, it is also apparent that there is more scatter in the observations than expected from the measurement errors. The errors ($\sim$ 3 ppm at g' band) are close to the highest precision achievable with the instrument.
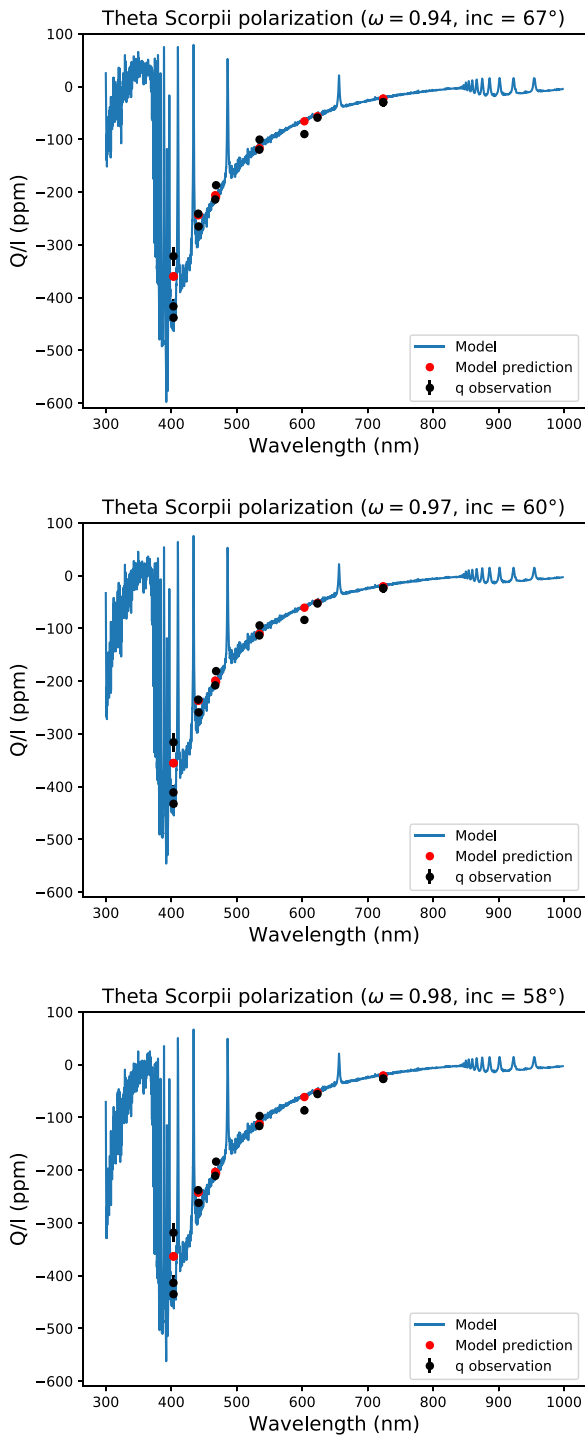
Figure 4. Wavelength dependence of polarization for θ Sco observations, with best-fitting polarimetric model results for selected inclinations. Black dots represent the observations, corrected for interstellar polarization, and rotated; polarimetric models are shown as blue curves (full models) and red points (passband-integrated). Rotation of the observational data points into the model reference frame serves to essentially zero the *u* Stokes parameter, leaving the polarization solely in the *q* component.

Under these circumstances, we begin to see effects arising from changes in the instrument configuration, and from the imperfect characterization of the low-polarization standard stars. In a more extensive study of polarization variability using these instruments (Bailey et al. 2021), we found evidence for zero-point differences between different observing runs by amounts of up to ∼10 ppm. These effects likely contribute to the scatter seen in the data. Any polarization variability in θ Sco over the period of observation will also contribute to the scatter.

2.1 Interstellar control stars

Dust in the interstellar medium (ISM) can have a significant effect on the observed polarization. To determine the intrinsic stellar polarization, it is therefore necessary to subtract the interstellar polarization, as part of the polarimetric modelling. The methodology can be tested by examination of normal stars thought not to be intrinsically polarized (Cotton et al. 2016). Cotton et al. (2017b) developed an analytical model of interstellar polarization of stars close to the Sun by using control stars within 35° of a target. Data for a number control stars suitable for use with θ Sco are available in the literature (Cotton et al. 2017b; Marshall et al. 2020; Piirola et al. 2020), and we have added to these through observations of the additional targets listed in Table 3.

3 THE BINARY θ SCO

3.1 Binarity revisited

See (1896) reported the discovery, from Lowell Observatory, of a visual companion to θ Sco A 'of the 13th magnitude', at a distance of 6″.2 in PA 322°. This would have been a challenging observation (the star's altitude would've been less than 12°), and Ayres (2018) highlighted a number of inconsistencies in the inferred properties of such a companion.

As part of the extensive pre-launch programme, See's observations were included in the *Hipparcos* preparatory data compilations. One of several possible solutions to the subsequent *Hipparcos* astrometry agrees quite well with See's report, and consequently was adopted in the final catalogue (van Leeuwen 2007), thereby appearing to confirm the historical measurements. (Although See's B-component magnitude estimate was much fainter than the *Hipparcos* value of ∼5^m – in fact, his companion should ostensibly have been too faint to be detected with the satellite – this could have been consistent with his propensity for overestimating binary-system brightness differences, often by large amounts.)

The agreement now appears to have been no more than an unfortunate coincidence; subsequent direct visual observations have verified neither See's report, nor its apparent partial confirmation by *Hipparcos*. As early as 1927, Innes (1927) included the 'discovery' in a list of rejected observations after he failed to confirm See's result. Of six rejected systems on the relevant page of the catalogue, four are attributed to See. More recently, visual observers Kerr, Frew & Jaworski (2006) concluded that 'the companion indicated by the *Hipparcos* data does not exist (since they would easily have detected it). Moreover, the companion reported by See has not been re-observed (by skilled observers using comparable equipment at better sites) and its existence is also in doubt.' New speckle-interferometry results, discussed below, also rule out a 6″.2 companion with a magnitude difference ΔI ≲ 7.5.

Although we believe that See's 'discovery' must now be disregarded, the *Hipparcos* photometric scans do, nevertheless, unam-

Table 1. Summary of observing runs and telescope-polarization (TP) calibrations.

Run	Date range[d] (UT)	Instr.	Tel.	f/	Ap. (arcsec)	Mod.	Filt.	Det.[e]	n	$\lambda_{\rm eff}$ (nm)	Eff. (per cent)	$q_{\rm TP}$ (ppm)	$u_{\rm TP}$ (ppm)
										Observations[b]		Calibration[c]	
2014MAY	2014-05-12	HIPPI	AAT	8	6.6	MT	g'	B	1	466.5	88.5	-43.3 ± 0.9	-53.2 ± 1.0
2017AUG	2017-08-12	HIPPI	AAT	8	6.6	BNS-E2	g'	B	0			-9.1 ± 1.5	-2.6 ± 1.4
2018MAR	2018-03-29 to 04-07	HIPPI-2	AAT	8*	15.7	BNS-E3	425SP	B	2	403.5	39.7	177.1 ± 2.8	25.1 ± 2.8
							500SP	B	2	441.5	70.5	142.6 ± 1.2	19.9 ± 1.2
							g'	B	1	467.4	82.6	130.1 ± 0.9	3.9 ± 0.9
							r'	R	1	633.4	81.1	113.3 ± 1.4	7.2 ± 1.4
							650LP	R	2	723.8	62.5	106.9 ± 1.9	10.4 ± 1.9
2018JUL	2018-07-25	HIPPI-2	AAT	8*	11.9	BNS-E4	425SP	B	1	403.4	38.2	-5.6 ± 6.4	19.8 ± 6.3
							V	B	1	534.5	95.4	-20.3 ± 1.5	2.3 ± 1.5
							r'	B	1	603.4	86.6	-10.4 ± 2.2	3.7 ± 2.2
2018AUG	2018-08-18	HIPPI-2	AAT	8*	11.9	BNS-E5	V	B	1	535.5	95.2	-20.3 ± 1.5	2.3 ± 1.5

The header row "Telescope and instrument set-up[a]" spans Instr. through Det. columns.

Note. ∗ Indicates use of a 2× negative achromatic lens, effectively making the foci f/16. [a]A full description, along with transmission curves for all the components and modulation characterization of each modulator ('Mod.') in the specified performance era, can be found in Bailey et al. (2020a). [b]Mean values are given as representative of the observations made of θ Sco. Individual values are given in Table 2 for each observation; n is the number of observations of θ Sco. [c]The observations used to determine the TP and the high-polarization standards observed to calibrate position angle (PA), and the values of $\sigma_{\rm PA}$ are described in Bailey et al. (2015) (MAY2014), Cotton et al. (2019) (AUG2017), and Bailey et al. (2020a) (other runs). [d]Dates given are for observations of θ Sco and/or control stars. [e]B, R indicate blue- and red-sensitive H10720-210 and H10720-20 photomultiplier-tube detectors, respectively.

Table 2. Polarization observations of θ Sco (sorted by effective wavelength).

Run	UT	Dwell (s)	Exp. (s)	Filt.	Det.[a]	$\lambda_{\rm eff}$ (nm)	Eff. (per cent)	q (ppm)	u (ppm)	p (ppm)	θ (°)
2018MAR	2018-03-29 16:32:03	1683	1280	425SP	B	403.5	39.8	-421.1 ± 13.3	32.5 ± 13.2	422.4 ± 13.3	87.8 ± 0.9
2018MAR	2018-04-07 17:17:10	1736	1280	425SP	B	403.3	39.6	-391.9 ± 13.2	-31.4 ± 13.2	393.2 ± 13.2	92.3 ± 1.0
2018JUL	2018-07-25 14:00:48	1064	640	425SP	B	403.4	38.2	-299.3 ± 16.5	-4.0 ± 16.4	299.3 ± 16.5	90.4 ± 1.6
2018MAR	2018-03-29 16:08:40	997	640	500SP	B	441.8	70.7	-242.0 ± 6.7	-0.7 ± 6.8	242.0 ± 6.8	89.9 ± 0.8
2018MAR	2018-04-07 17:43:55	1185	730	500SP	B	441.2	70.3	-217.0 ± 6.6	-4.9 ± 6.8	217.1 ± 6.7	90.7 ± 0.9
2014MAY	2014-05-12 18:54:11	1257	720	g'	B	466.5	88.5	-164.2 ± 3.2	12.4 ± 3.3	164.7 ± 3.2	87.8 ± 0.6
2018MAR	2018-03-29 15:51:38	986	640	g'	B	467.2	82.5	-192.6 ± 2.8	22.9 ± 2.8	194.0 ± 2.8	86.6 ± 0.4
2018JUL	2018-07-25 13:24:11	1072	640	V	B	534.5	95.4	-96.3 ± 4.1	17.3 ± 4.2	97.8 ± 4.2	84.9 ± 1.2
2018AUG	2018-08-18 14:36:26	973	640	V	B	534.9	95.2	-78.0 ± 4.0	25.2 ± 4.4	82.0 ± 4.2	81.0 ± 1.5
2018JUL	2018-07-25 13:42:18	1045	640	r'	B	603.4	86.6	-66.7 ± 7.0	17.1 ± 7.1	68.9 ± 7.0	82.8 ± 2.9
2018MAR	2018-04-01 16:47:55	1001	640	r'	R	623.4	81.1	-37.5 ± 3.8	33.4 ± 3.5	50.2 ± 3.6	69.2 ± 2.1
2018MAR	2018-04-01 17:05:16	1012	640	650LP	R	723.8	62.5	-9.3 ± 5.5	35.5 ± 4.8	36.7 ± 5.2	52.3 ± 4.3
2018MAR	2018-04-01 17:24:21	1162	800	650LP	R	723.8	62.5	-12.1 ± 7.4	51.7 ± 6.0	53.1 ± 6.7	51.6 ± 3.9

[a]B, R indicate blue- and red-sensitive H10720-210 and H10720-20 photomultiplier-tube detectors, respectively.

Table 3. Observations of interstellar-control stars.

Control HD	SpT	Run	UT	Dwell (s)	Exp. (s)	$\lambda_{\rm eff}$ (nm)	Eff. (per cent)	q (ppm)	u (ppm)	p (ppm)	θ (°)
HD 131342	K2III	2018MAR	2018-03026 14:22:44	1716	1280	475.8	86.1	17.9 ± 6.6	29.9 ± 6.7	34.8 ± 6.6	29.6 ± 5.5
HD 138538	K1/2III	2018AUG	2018-09-01 09:00:57	961	640	475.6	65.0	14.9 ± 12.2	-20.4 ± 8.6	25.2 ± 10.4	153.0 ± 13.5
HD 147584	F9V	2018AUG	2018-08-20 13:35:24	967	640	471.9	74.8	30.5 ± 7.9	-13.3 ± 9.1	33.2 ± 8.5	168.2 ± 7.5
HD 160928	A3IVn	2018MAR	2018-03-29 17:03:49	1721	1280	462.9	80.7	36.0 ± 7.6	-17.2 ± 7.9	39.9 ± 7.7	167.2 ± 5.6
		2018MAR	2018-03-29 17:32:31	1695	1280	462.8	80.6	23.3 ± 7.8	-5.6 ± 7.5	23.9 ± 7.7	173.2 ± 9.7
HD 153580	F5V	2018AUG	2018-09-01 09:28:47	3852	1040	468.5	60.7	14.8 ± 9.7	30.8 ± 10.5	34.2 ± 10.2	32.2 ± 8.9
HD 166949	G8III	2018MAR	2018-03-30 16:19:18	1704	1280	474.6	85.6	4.4 ± 12.2	10.8 ± 12.3	11.7 ± 12.3	34.0 ± 32.8
		2018MAR	2018-03-30 16:47:44	1709	1280	474.6	85.6	-0.7 ± 12.5	-17.7 ± 11.7	17.8 ± 12.1	133.9 ± 24.1
HD 169586	G0V	2017AUG	2018-08-12 15:01:10	4252	3200	473.1	89.3	155.7 ± 11.0	5.0 ± 10.5	155.8 ± 10.8	0.9 ± 1.9
HD 174309	F5	2018MAR	2018-03-30 18:33:06	1715	1280	467.1	82.5	-138.2 ± 9.4	-200.3 ± 9.6	243.3 ± 9.5	117.7 ± 1.1
HD 182369	A4IV	2018MAR	2018-03-23 18:29:51	1108	640	463.6	81.0	-120.3 ± 7.5	-9.4 ± 7.1	120.6 ± 7.3	92.2 ± 1.7

Note. All control-star observations were made with the SDSS g' filter and B photomultiplier tube. The same aperture as used for the θ Sco observations in the same run was used. Spectral types (SpT) are from SIMBAD.

biguously indicate a visual binary (and, in effect, now represent the discovery of a companion). We have therefore re-examined the raw *Hipparcos* scans to investigate alternative solutions, using an S-type differential analysis (cf. section 4.1.3 of van Leeuwen 2007).

While this paper was in preparation our work prompted new speckle interferometry with HRCam at SOAR (Tokovinin 2018). The results (in particular, Δm) favour the new *Hipparcos* solution that is listed in Table 4, together with the average of four HRCam observations obtained on two nights a month apart (Tokovinin, personal

Table 4. New astrometric results, discussed in Section 3.1. Magnitude differences are ΔH_{P} (*Hipparcos*) and $\Delta y/I$ (HRCam).

Parameter		*Hipparcos*	HRCam
Epoch	yr (CE)	1991.25	2021.6
θ_{B}	$^{\circ}$	274.3 ± 0.13	97.54 ± 0.78
ρ	$''$	0.538 ± 0.003	0.2447 ± 0.0025
Δm	mag	3.27 ± 0.01	3.32/3.69
$\mathrm{d}\theta_{\mathrm{B}}/\mathrm{d}t$	$^{\circ}$/yr	-3.385 ± 0.139	
$\mathrm{d}\rho/\mathrm{d}t$	$''$/yr	-0.0257 ± 0.0021	
π	mas	9.90 ± 0.26	

Table 5. Best-fitting values of the inclination i and their 1σ uncertainties, at selected values of the rotation parameter, ω.

ω	i (degrees)
0.99	55.54 ± 0.79
0.98	58.01 ± 0.87
0.97	60.09 ± 1.03
0.96	62.61 ± 1.03
0.95	65.31 ± 1.21
0.94	67.34 ± 1.35

communication). This new *Hipparcos* solution is consistent with results of the visual double-star observers, and the inferred parallax is significantly more precise than the original 'new reduction' result.

3.2 The companion

With its sub-arcsecond separation, the secondary was certainly included in the aperture of all photopolarimetric observations considered in this paper. Its properties are therefore of interest, if only for its potential as a contaminant.

Assuming, as a starting point, that $\Delta V = \Delta H_{\mathrm{P}}$, then a system magnitude of $V = 1.87$ (Johnson et al. 1966) implies $V_{\mathrm{A,B}} = 1.92$, 5.19, and provisional $M(V)$ values of -3.12, $+0.16$ (for parallax $\pi = 9.90$ mas and differential extinction $E(B-V) = 0^{\mathrm{m}}005$; Section 4.2).

The secondary's absolute magnitude corresponds, very roughly, to spectral classifications ∼B8 V, A0 IV, or A3 III (e.g. Gray & Corbally 2009; brighter luminosity classes are excluded). On that basis, we can next apply a differential-colour correction to the *Hipparcos* photometry, taking $(V-I) \simeq +0.55$, $+0.10$ for the primary and secondary (observed and inferred; Johnson et al. 1966, Ducati et al. 2001). Using the $(V-H_{\mathrm{P}})$, $(V-I)$ calibration from Bessell (2000), we obtain $\Delta V \simeq \Delta H_{\mathrm{P}} + 0^{\mathrm{m}}07 = 3.34$ ($V_{\mathrm{A,B}} = +1.92$, $+5.26$), and final $M(V)$ values of -3.12 ± 0.06, $+0.22 \pm 0.06$, where the 1σ ranges, derived from a simple Monte Carlo analysis, incorporate the formal errors on the parallax (which remains the major source of uncertainty) and on ΔH_{P}, an assumed uncertainty of 0.01 on V, and a uniform distribution in $E(B-V)$ of 0:0.01 (Section 4.2).

There is no detectable flux shortwards of 1500 Å in spectra obtained with the *International Ultraviolet Explorer*, *IUE* (Section 4.2; the secondary would certainly have been included in these observations), implying $T_{\mathrm{eff}} \lesssim 8.5\mathrm{kK}$ (spectral type ∼A3 or later), whence $R \gtrsim 4\,\mathrm{R}_{\odot}$ in order to match $M(V)$. The secondary's properties therefore appear to be broadly consistent with an ∼A3 giant star. The HRCam Δm results in Table 4 are quantitatively consistent with such a companion.
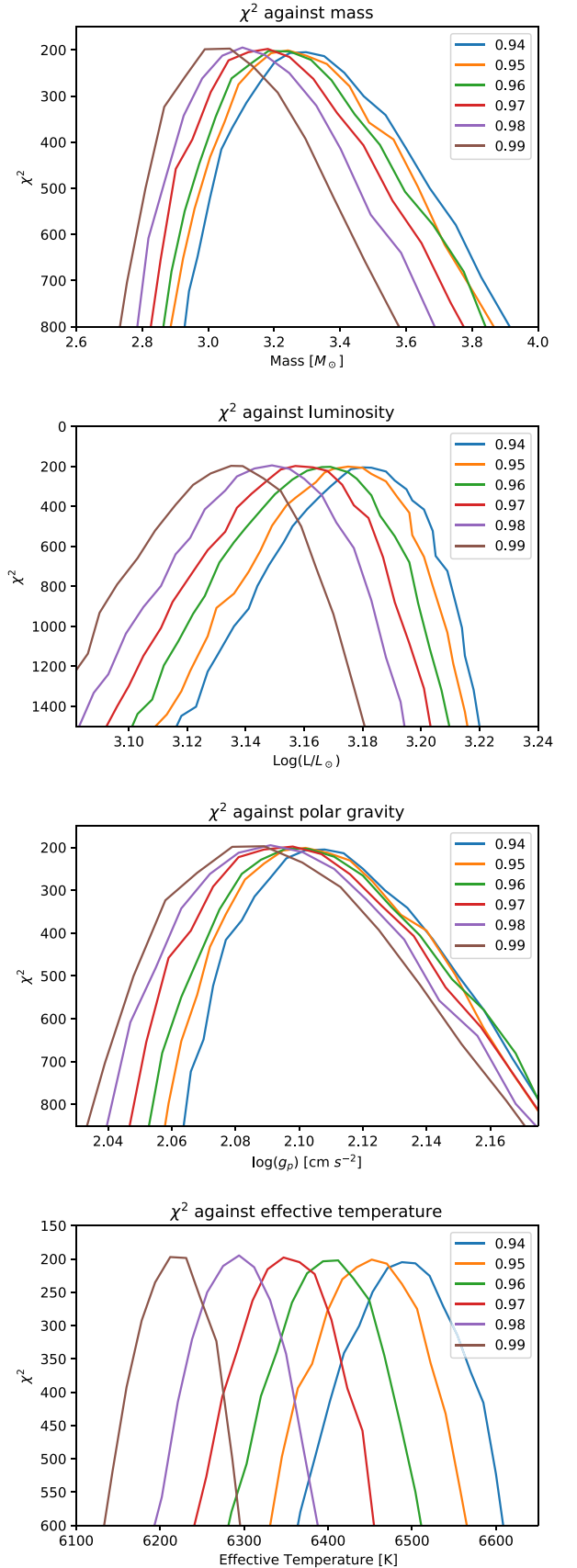
Figure 5. Various stellar parameters plotted against χ^2 values. Each plotted line represents a unique omega value as designated in the legend.

Table 6. Best-fitting θ Sco A parameters. The final column lists results from Domiciano de Souza et al. (2018, their table 2, ω-model results), discussed in Section 5.4.

Stellar parameter	This work	DdeS	
Inclination, i [°]	58^{+9}_{-3}	$61.8^{+0.8}_{-0.9}$	
ω	≥ 0.94	0.845 ± 0.008	[1]
T_{eff} [K]	6294^{+224}_{-111}	6235^{+7}_{-8}	[2]
$\log(L/L_\odot)$	$3.149^{+0.041}_{-0.028}$	3.041 ± 0.006	[1]
R_{e} [$R_\odot$]	$35.5^{+1.5}_{-2.3}$	$30.30^{+0.08}_{-0.09}$	
R_{p} [$R_\odot$]	26.3 ± 0.9	25.92 ± 0.09	[1]
Mass [$M_\odot$]	$3.10^{+0.37}_{-0.32}$	$5.09^{+0.13}_{-0.14}$	
$\log(g_{\mathrm{p}})$[dex cgs]	$2.091^{+0.042}_{-0.039}$	2.317 ± 0.012	[1]
P_{rot} [days]	$16.60^{+0.96}_{-1.03}$	14.74 ± 0.16	[1]
θ_* [°]	3.3 ± 1.0	$182.1^{+0.5}_{-0.4}$	
Interstellar-polarization parameter			
p_{i} [ppm]	$43.7^{+6.2}_{-3.9}$		
θ_{i}[°]	$32.6^{+5.8}_{-5.2}$		

Notes. θ_* is the PA of the stellar rotation axis, and θ_{i} is the PA of interstellar polarization; both have a $\pm 180°$ ambiguity in the case of the polarimetry (i.e. θ_* can be 183.3° or 3.3°).
[1] Uncertainty estimated by propagation of errors from data given by Domiciano de Souza et al., assuming $\sigma(R_{\mathrm{p}}) \simeq \sigma(R_{\mathrm{e}})$ where necessary.
[2] Domiciano de Souza et al. quote an 'average effective temperature', presumably $\int T_{\mathrm{eff}}^\ell \, \mathrm{d}A / \int \mathrm{d}A$, where T_{eff}^ℓ is the local effective temperature and $\mathrm{d}A$ is an element of surface area. We have corrected this to match our definition, $\sigma_{\mathrm{B}} T_{\mathrm{eff}}^4 = L / \int \mathrm{d}A$.

3.3 The orbit

The pair's angular separation at the *Hipparcos* epoch corresponds to a projected centres-of-mass separation of 54 au ($\sim 11\,600$ R$_\odot$; orbital period $\sim 180(a/54 \text{ au})^{3/2}/\sqrt{\Sigma M/5\text{M}_\odot}$ yr, where a is the semimajor axis and ΣM is the sum of the masses). The observations are insufficient to further constrain the orbital parameters, but the system appears to be wide in the sense that the B component is unlikely to have affected the primary's evolution.

4 MODELLING

4.1 Polarization

Our approach to modelling the polarization of a rotating star follows that previously used for α Oph (as described in detail by Bailey et al. 2020b) and Regulus (Cotton et al. 2017a). We use a Roche model, with the variation of temperature over the stellar surface following from the gravity-darkening law of Espinosa Lara & Rieutord (2011). A rectangular grid of pixels is overlaid on the projected geometry, for given axial inclination i and rotation ω ($=\Omega/\Omega_{\mathrm{c}}$, where Ω_{c} is the critical angular rotation rate at which the centrifugal force balances gravity at the equator). For each pixel, the local stellar temperature, gravity, and surface-normal viewing angle are calculated, and used to determine the intensity and polarization, as a function of wavelength. Summing all the pixels gives the total intensity and polarization as a function of wavelength. The model coordinate frame is aligned with the rotation axis of the star in the plane of the sky, so that all the integrated polarization remains in the q Stokes parameter (with the u polarization being essentially zero).

The local intensity and polarization are interpolated from ATLAS9 solar-composition stellar-atmosphere models computed for the local effective temperatures and gravities at 46 colatitudes, from 0° to 90°

at 2° intervals. For each model atmosphere, the specific intensity and polarization are computed using a version of the SYNSPEC spectral synthesis code (Hubeny, Stefl & Harmanec 1985; Hubeny 2012) modified to do a fully polarized radiative-transfer calculation, using the VLIDORT code of Spurr (2006).

The final integrated polarization results are then corrected to allow for the small contribution of the companion to the intensity. The companion is assumed to have a temperature of 8000 K and to have no intrinsic polarization.

4.2 Stellar parameters

The predicted polarization depends on four main parameters: the rotation rate (ω), a reference temperature and gravity (e.g. polar values T_{p}, g_{p}), and the axial inclination (i). We use additional observational information to provide relationships between these parameters, thereby reducing a 4D space to a 2D grid. We take the projected equatorial rotation speed $v_{\mathrm{e}}\sin i$ and distance d (which together constrain ω), and the spectral-energy distribution (which constrains the temperature). Then, for any specified (ω, i) pairing, we can determine the (temperature, gravity) values that are uniquely consistent with all constraints, as described in detail in our study of α Oph (Bailey et al. 2020b),

For simplicity (and with no important loss of information or sensitivity), we use the ratio of ultraviolet (UV) to V-band fluxes to determine the temperature. The UV fluxes are from archival *IUE* spectra (SWP 48384 and LWP 26146, the only low-resolution, large-aperture spectra available), from which we obtain an observed 120–301 nm integrated flux of 9.85×10^{-8} erg cm^{-2} s^{-1}. We apply two corrections: first, extinction for $E(B-V) = 0^{\mathrm{m}}005$ (based on the magnitude of the interstellar polarization; Section 5), with a Seaton (1979) extinction law. Secondly, we subtract an estimated B-component flux, based on an 8.0kK, $\log g = 4.0$ model, from Howarth (2011), scaled to the secondary's (dereddened) V magnitude. The corrections are each smaller than 10 per cent of the observed flux, and act in opposite directions. We explore the dependence of the final results on the exact values as part of our sensitivity analysis (Section 5.2).

We also use the V-band results obtained in Section 3.2, and the *Hipparcos* distance of 101.0 pc (Section 3.1; the star is too bright to be included in *Gaia* data releases available at the time of writing). Finally, we adopt $v_{\mathrm{e}}\sin i = 91.7$ km s^{-1} from Domiciano de Souza et al. (2018); we verified the plausibility of this value (and were unable to improve on it) by comparing synthesized spectra to an archival UVES spectrum obtained with the VLT.

The resulting model grid for θ Sco A is illustrated in Fig. 2. The grid covers ω from 0.8 to 0.99 in steps of 0.01 (only half these points are plotted on the figure), and inclinations from 45 to 90 deg in 1-deg steps (only values at 5-deg steps are plotted on the figure). Each point in the grid represents a model star that reproduces the observed UV and V flux levels (and the overall flux distribution) for the adopted d, $v_{\mathrm{e}}\sin i$ and the specified i, ω.

5 RESULTS

The polarization modelling described in Section 4.1 provides predictions of the wavelength dependence of polarization for each of the models in the grid described in Section 4.2. We compare these predictions to the observed polarization, corrected for interstellar polarization, to determine which model or models in the grid best match the data.

Table 7. Parameter sensitivity to fixed inputs, showing differences (model minus base) with respect to a reference model having $\omega = 0.98$, $i = 58°$, $v_e\sin i = 91.7$ km s^{-1}.

Parameter	Unit	Base value	Parallax		UV flux		$v_e\sin i$	
			$+1\sigma$	-1σ	$\times 0.95$	$\times 1.05$	-5 km s^{-1}	$+5$ km s^{-1}
$R_p/R_\odot$		26.272	-0.658	$+0.614$	$+0.614$	-0.599	-0.223	$+0.129$
$R_e/R_\odot$		35.475	-0.890	$+0.828$	$+0.828$	-0.810	-0.302	$+0.173$
$\log(g_p)$	dex cgs	2.091	$+0.011$	-0.010	-0.010	$+0.010$	-0.045	$+0.044$
T_{eff}	kK	6.294	-0.004	$+0.005$	-0.063	$+0.062$	$+0.019$	-0.018
$M/M_\odot$		3.104	-0.078	$+0.073$	$+0.073$	-0.071	-0.354	$+0.365$
$\log L/L_\odot$		3.149	-0.023	$+0.022$	$+0.003$	-0.003	-0.002	$+0.000$

Note. It may appear that, in principle, T_{eff} should be independent of parallax; in practice, small changes in the inferred gravity (and hence emergent model fluxes) result in changes of a few kelvin with distance.

To make the comparison, we integrate the model polarization over each filter bandpass (Bailey et al. 2020a). Since the model polarizations are entirely in the q Stokes parameter, by aligning the observed and model polarization vectors we also determine the PA of the star's rotation axis.

5.1 Interstellar polarization

Interstellar polarization results from dichroic scattering of light by aligned, non-spherical dust grains along the line of sight (Davis & Greenstein 1951). It has a distinctive wavelength dependence, generally well approximated by the 'Serkowski law':

$$\frac{p(\lambda)}{p_{max}} = e^{[-K\ln^2(\lambda_{max}/\lambda)]} \tag{1}$$

(Serkowski 1971, 1973; Serkowski, Mathewson & Ford 1975), where $p(\lambda)$ is the polarization at wavelength λ and p_{max} is the maximum polarization, occurring at wavelength λ_{max}. The normalizing constant K has been found to be linearly related to λ_{max} (Wilking et al. 1980); Whittet et al. (1992) give

$$K = (0.01 \pm 0.05) + (1.66 \pm 0.09)\lambda_{max}, \tag{2}$$

where λ_{max} is in μm.

Because the wavelength dependence of the interstellar polarization is quite different to that of the rotational polarization it is possible to determine interstellar-polarization parameters in parallel with the fitting of stellar models to the observations. For each model in the grid, we determined the difference between the modelled and observed polarization for each filter and fit a Serkowski curve, equation (1), to these differences. The fits were carried out using the CURVE_FIT routine of the PYTHON package SCIPY (Jones et al. 2001).

Although values for λ_{max} around 470 nm or less have been found for stars near to the Sun (Marshall et al. 2016, 2020; Cotton et al. 2019; Bailey et al. 2020b), θ Sco, at $d \simeq 100$ pc, is near to the wall of the Local Hot Bubble, which is associated with a value of 550 nm (Cotton et al. 2019) – this is also a typical value for the Galaxy as determined by Serkowski et al. (1975) and Whittet et al. (1992). Consequently, we fixed λ_{max} to 550 nm, which in turn fixes K (equation 2). This leaves three fit parameters: p_i (equivalent to p_{max}, but for fixed λ_{max}), θ_i (the PA of the interstellar polarization), and θ_* (the PA of the star's rotation axis).

5.2 Results: stellar parameters

Fit quality across the model grid was characterized by χ^2, shown in Fig. 3. There is no single, well-defined χ^2 minimum; rather, a locus of low-χ^2 values runs across a rough diagonal in the ω/i plane, since these two parameters have similar effects on the polarization curve. Fig. 4 compares observed and modelled polarizations at several points along the χ^2 'valley' to illustrate this near-redundancy. The minimum-χ^2 grid point is at $\omega = 0.98$, $i = 58°$, but well-fitting models (within 1σ of the global minimum) can be identified at all $\omega \gtrsim 0.94$.

Parameter uncertainties were estimated through bootstrapping (i.e. resampling with replacement; e.g. Press et al. 2007), for ω values encompassing the 1σ range of best-fitting χ^2 results (Table 5). At each ω, a precise best-fitting inclination was determined by spline interpolation in χ^2, and its 1σ uncertainty estimated through 1000 bootstrapped replications. The resulting $\Delta\chi^2$ was then used to estimate errors on other parameters (cf. Fig. 5). Results are summarized in Table 6. An advantage of this bootstrap procedure is that it bases the error determinations on the actual scatter in the data, rather than on the formal measurement errors that, as noted in Section 2, may be underestimated.

In addition to the statistical errors addressed by the foregoing procedures, systematic errors in parameter estimates will arise if the values adopted for observational constraints in Section 4.2 are incorrect. We conducted simple sensitivity tests, the results of which are summarized in Table 7. As a baseline model, we adopted the minimum-χ^2 grid point ($\omega = 0.98$, $i = 58°$) and varied the parallax, UV flux, and $v_e\sin i$ over reasonable ranges. There are also smaller second-order effects resulting from displacements of the χ^2 valley (Fig. 3) with changing inputs. We estimated the additional errors due to these effects and added them in quadrature to the statistical errors from the bootstrap analysis to obtain the uncertainties listed in Table 6.

One of the stellar parameters determined is the rotation period of the star, P_{rot}, for which we obtain 16.60 $^{+0.96}_{-1.03}$ d. θ Sco is not known to be a variable star. It is not listed in the General Catalogue of Variable Stars (Samus' et al. 2017). We have examined the available space photometry from *Hipparcos* and *TESS* (*Transiting Exoplanet Survey Satellite*; Ricker et al. 2015) and see no evidence for variability on the rotation period or any shorter period. θ Sco does not therefore show the periodic variability seen in some other rapidly rotating stars, in particular Be stars, and attributed to either non-radial pulsations (e.g. Baade et al. 2016) or rotational modulation (Balona & Ozuyar 2020).

5.3 Results: interstellar polarization parameters

The interstellar polarization parameters determined through the χ^2 analysis can be checked through comparison with the interstellar polarizations of control stars within 35° of θ Sco, illustrated in Fig. 6. This region of the ISM is contained within the Local Hot Bubble,
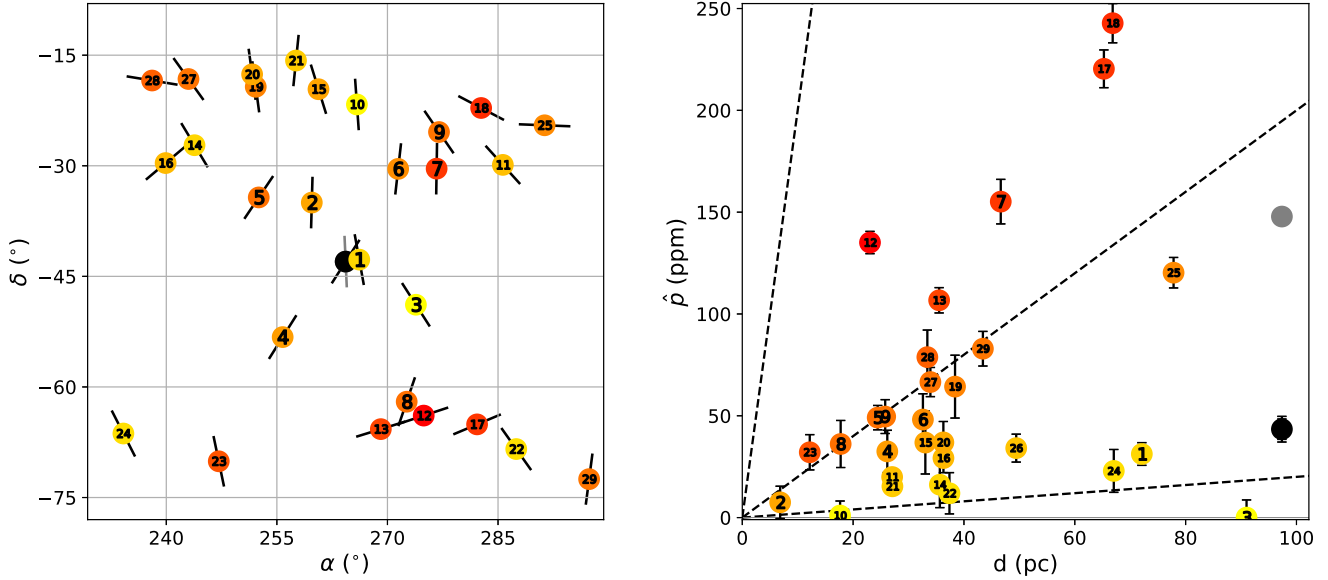
**Figure 6.** Map (left) and p versus d plot (right) of interstellar control stars within $35°$ of θ Sco. The control distances and co-ordinates were taken from SIMBAD. Black pseudo-vectors on the data points indicate the PAs (θ_i), but not the magnitudes, of the interstellar polarizations. The effective wavelengths of the control observations have been used to standardise each to a wavelength of 450 nm (roughly corresponding to g$'$), assuming a λ_{max} of 470 nm – which is appropriate since all are closer than θ Sco and thus probably not in the 'wall' of the Local Hot Bubble (Cotton et al. 2019). The controls are colour coded in terms of $\hat{p}/d$ and numbered in order of their angular separation from θ Sco; they are: 1: HD 160928, 2: HD 156384, 3: HD 166949, 4: HD 153580, 5: HD 151680, 6: HD 165135, 7: HD 169586, 8: HD 165499, 9: HD 169916, 10: HD 160915, 11: HD 176687, 12: HD 167425, 13: HD 162521, 14: HD 146070, 15: HD 157172, 16: HD 143114, 17: HD 173168, 18: HD 174309, 19: HD 151504, 20: HD 151192, 21: HD 155125, 22: HD 177389, 23: HD 147584, 24: HD 138538, 25: HD 182369, 27: HD 131342, 28: HD 145518, 29: HD 147766, 30: HD 141937, 31: HD 186219. In the p versus d plot dashed lines corresponding to $\hat{p}/d$ values of 0.2, 2.0, and 20.0 ppm/pc are given as guides. The grey data point is derived from the interstellar model in Cotton et al. (2017b) and the black data point represents our best-fitting interstellar values for θ Sco.

which extends ∼75–150 pc around the Sun and which has little dust, very patchily distributed (Bailey, Lucas & Hough 2010; Frisch et al. 2010; Cotton et al. 2019). The patchiness means that control-star observations cannot be used to determine the interstellar values for θ Sco directly, but they can test whether the model values (Table 6) are reasonable. Fig. 6 shows that the polarization PAs of stars between declinations -30 and $-60°$ are roughly aligned to $0 \pm 45°$, consistent with the value found for θ Sco; while the magnitude of the inferred interstellar polarization for θ Sco is similar to its closest neighbour on the sky, HD 160928.

Finally, we note that the magnitude of the rotationally induced stellar polarization exceeds the interstellar component at all observed wavelengths, and dominates in the blue.

5.4 Comparison with interferometry

Domiciano de Souza et al. (2018) conducted a detailed study of θ Sco A, using optical interferometry supplemented with high-resolution spectroscopy. A comparison of our results with theirs shows disappointingly poor agreement for the inferred masses, and for other key stellar parameters (Table 6; Fig. 3). The small difference in adopted distances does not account for the discrepancies (cf. Table 7); nor are they attributable to contamination of the interferometric observations by the B component. [Even if the then-unknown secondary was within the effective field of view of the interferometric instrumentation, ∼0.′′12–0.′′15, at the time of observations (2016), it would not be expected to influence the interferometric results strongly; Domiciano de Souza, personal communication.]
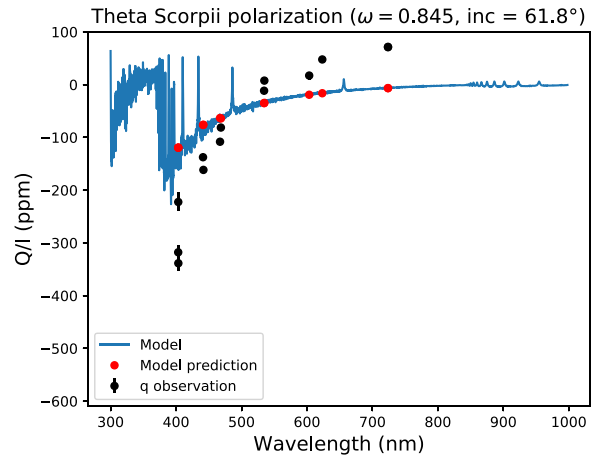
Figure 7. Wavelength dependence of polarization for θ Sco observations (as Fig. 4) compared with a polarization model based on the parameters of Domiciano de Souza et al. (2018). Black dots represent the observations, corrected for interstellar polarization and rotated; polarimetric models are shown as a blue curve (full models) and red points (passband-integrated).

We have been unable to identify any aspects of our analysis that are likely to account for the differences. In particular, the observed polarization cannot be reproduced without near-critical rotation ($\omega \gtrsim 0.9$; Fig. 3), which requires $M \sim 3\,M_\odot$. Fig. 7 shows the intrinsic polarization predicted by our model for the Domiciano de Souza et al. parameter set ($\omega = 0.845$; we quote numerical results from the 'ω-model' solution given in table 2 of Domiciano de Souza et al. 2018,

for consistency with our analysis). Comparison with observations shows differences that are too large to be accommodated by stochastic errors, or by plausible uncertainties in polarization arising in either the ISM or, potentially, the B component.

Although it is, of course, possible that our modelling code is in error, it has been tested against independent third-party calculations without giving any cause for concern (Cotton et al. 2017a). There are, however, indications that the posterior probability distributions generated by the Domiciano de Souza et al. MCMC model-fitting procedure may not be fully reliable. For example, a distance of 91.16 ± 12.51 pc was used as a prior in their analysis; since the interferometry gives, essentially, an angular-diameter measurement, we would expect uncertainties on inferred radii of not less than $12.51/91.16 \simeq 14$ per cent, yet the quoted error on R_e is actually < 0.3 per cent.

The Domiciano de Souza et al. T_{eff} determination, 6215^{+7}_{-8} K also appears to be remarkably precise for a measurement based on the synthesis of only a 26-nm stretch of rectified spectrum, and while they give no error on $v_e \sin i$ – which, like T_{eff}, must be constrained primarily by spectroscopy – the upper limit given by $\sigma(v_e)$, $\simeq 1.0$ km s^{-1}, again seems unexpectedly small.

[Domiciano de Souza et al. (2018) separately list results based solely on interferometry in their table 3, which includes values for the equatorial rotation velocity with stated accuracies of ~10 per cent; it is unclear to us how this parameter can be determined at all using only interferometry. Other parameter values quoted in the table as 'not constrained' are indeed completely indeterminate from interferometry alone, so that the numerical values given there, and their uncertainties, are arbitrary.]

Our own spectrum-synthesis calculations show that rectified spectra computed for ±1σ changes in T_{eff} or v_e differ by ~0.2 per cent in the core of Hα (and by much less elsewhere), which is an order of magnitude smaller than the corresponding O−C (or likely rectification uncertainties), and is comparable to the purely statistical errors in the observed spectra. Even as purely formal errors, we therefore suspect that the quoted T_{eff} and v_e uncertainties may also be unrealistically small.

If measures of dispersion in at least some of the posterior distributions determined by Domiciano de Souza et al. (2018) are indeed too small, then measures of central tendency (i.e. parameter values) may also be open to question. This is difficult to scrutinize directly since Domiciano de Souza et al. delegated basic observables (such as angular diameters) to derived quantities, for which they did not propagate uncertainties.

5.5 The potential utility of UV polarimetry

As discussed in Section 5.2, i and ω are not separately well constrained for θ Sco (nor for α Oph, for which the situation is worse; Bailey et al. 2020b), because these parameters have similar effects on the polarization curve over the wavelength range sampled. In this section, we briefly examine prospects for resolving this redundancy through observations in the UV, such as allowed by the proposed *Polstar* mission (Scowen et al. 2021) – which has been suggested for these types of observations (Jones et al. 2021).

To this end we ran a SYNSPEC/VLIDORT model for each 5° increment from table 4 of Bailey et al. (2020b) for α Oph, and from Table 5 of this paper for θ Sco, using appropriate ω, i values as listed there, with T_{eff} and $\log(g_p)$ interpolated in the model grid in inclination for α Oph and in ω for θ Sco. The models were run over the wavelength range 100–300 nm, using the UV line lists 'gfFUV' and 'gfNUV' acquired

from the SYNSPEC website and originally computed by Kurucz & Bell (1999).

The results of the modelling are shown in Fig. 8. Below 300 nm Q/I becomes increasingly more negative (the model U/I is essentially zero; Section 4.1); this is similar to results for the highly inclined B-type stars modelled to 250 nm by Sonneborn (1982), and much further into the UV by Collins, Truax & Cranmer (1991). Polarization increases considerably with decreasing wavelength, reaching a few per cent before the flux becomes negligible.

For α Oph we see that, although the 85° and 90° models are nowhere easily separated, there are two regions that appear promising for distinguishing between the models at either end of the inclination range. In the longer wavelength end of the range the low-inclination models are more polarized; between 200 and 240 nm the difference in polarization between the 60° and 90° models is roughly 100 ppm. Shortward of 180 nm, where the higher inclination models are the more polarized, the difference between extreme inclinations is 1 per cent (10^4 ppm), though the very low flux here presents an impediment to utilizing this region in practice for all but the brightest stars.

Models of θ Sco that are indistinguishable in the optical begin to diverge between 350 and 300 nm (Fig. 4); this trend continues down to the Mg II absorption lines at ~280 nm (Fig. 8), where the lowest inclination model exhibits around 200 ppm more polarization than the highest inclination model, making this a promising region for study. Some small (10–20 ppm) divergence in this region is also seen for α Oph. However, it is much stronger in θ Sco, in part because it has lower gravity and is more polarized in general.

Between 230 and 280 nm the various θ Sco models are indistinguishable. Shortward of this range the higher inclination models exhibit more polarization, such that below 190 nm the models are again distinct across the entire inclination range, at first differing by a fraction of a per cent, rising to a few per cent at 170 nm; however, as an F-type star, the flux in this region is at best ~5 per cent of what it is at 300 nm.

6 EVOLUTIONARY STATUS

A major objective of this work was to measure the rotation of θ Sco A in order to investigate its evolutionary state, particularly through the examination of the rather precisely determined gravity. A comparison with rapidly rotating stellar-evolution models (Eggenberger et al. 2008; Georgy et al. 2013) is shown in Fig. 9, using the $\log(g_p)/\omega$ plane. Observed values (from Table 6) are compared to evolutionary tracks for zero-age main sequence (ZAMS) masses of 3 and 5 M$_\odot$ (at a range of initial rotation rates), reflecting our mass estimate (3.07 M$_\odot$) as well as higher values reported in the literature (Domiciano de Souza et al. 2018).

It is evident from Fig. 9 that θ Sco is rotating much faster than is consistent with any of the single-star evolutionary models. Even if it were born with critical rotation, its rotation rate would have dropped to $\omega = 0.4$ or less by the time it reached the evolutionary stage indicated by its $\log(g_p)$. This conclusion holds even for the somewhat lower rotation rate obtained by Domiciano de Souza et al. (2018) from interferometry.

The conflict with single-star evolutionary tracks is further demonstrated by a standard H–R diagram (Fig. 10). Based on single-star evolution one would infer that θ Sco A is in the Hertzsprung gap and more massive than 5 M$_\odot$ (cf. Domiciano de Souza et al. 2018). However, the mass determined from the polarization analysis is significantly lower than this.
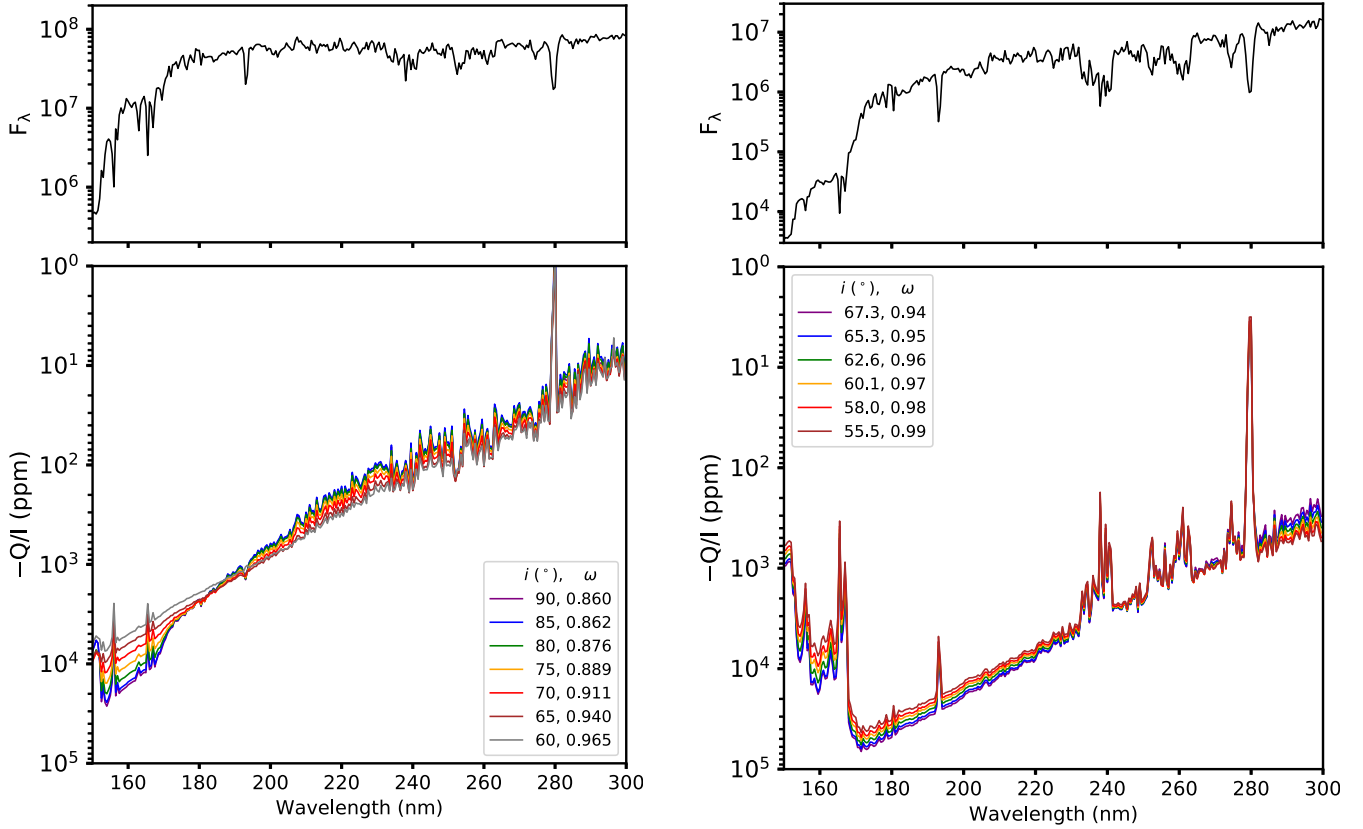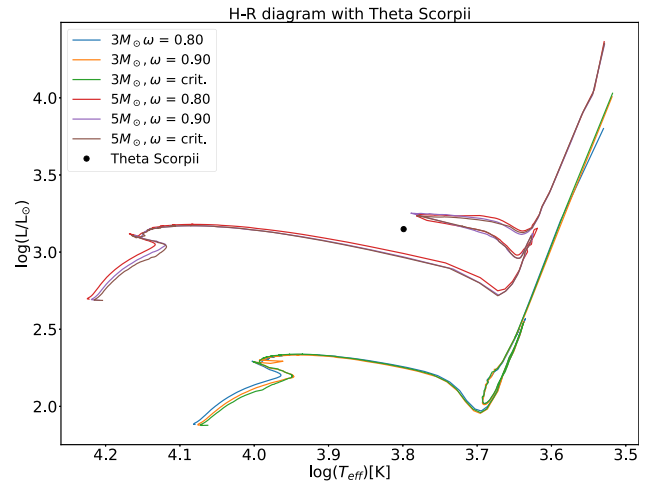
Figure 8. Left-hand panels: theoretical UV surface fluxes, F_λ, for α Oph (top, in units of erg cm^{-2} s^{-1} Å^{-1}), binned to 0.5 nm; and polarization spectra (bottom), corresponding to the optical models given in table 4 of Bailey et al. (2020b; coloured lines). Note that the abscissa of both panels are on log scales, with the most negative Q/I values at the bottom of the lower panel. Right-hand panels: same, but for θ Sco. Polarization spectra are shown for each of the models given in Table 5 of this paper.
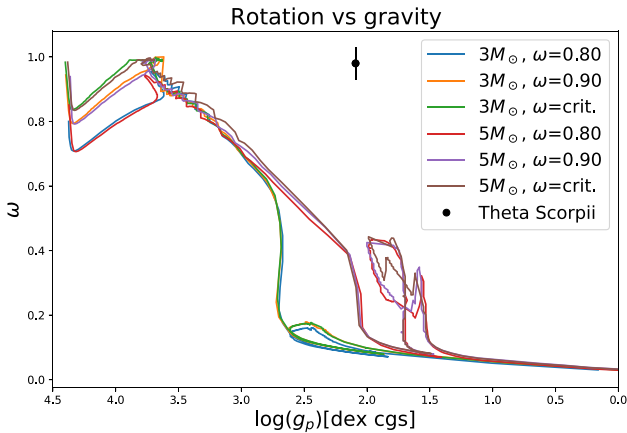
Figure 9. Evolutionary tracks in the log (g_p)/ω plane, using solar-abundance models from Georgy et al. (2013). Tracks are identified by mass and rotation rate on the ZAMS; evolution progresses from upper left to lower right on this plot. Our empirical result for θ Sco A is shown as a filled black dot with an error bar in ω [the formal uncertainty in log (g_p) is comparable to the dot size].

Figure 10. The position of θ Sco A in the H–R diagram, with evolutionary tracks for 3 and 5 M$_\odot$ stars.

These inconsistencies strongly suggest that θ Sco has followed a different evolutionary path to those described by single-star models. A likely scenario is that θ Sco A was initially a close binary system that has interacted and merged to reach its current state. The existence

of such stars is not surprising. Binaries are common among massive stars (Duchêne & Kraus 2013) and interactions and mergers are expected to be important factors in evolution (Sana et al. 2012; de Mink et al. 2013). It has been suggested that binary interaction may play a role in the rapid rotation of some Be stars (Pols et al. 1991; de Mink et al. 2013) and may be the predominant channel

for Be star formation (Bodensteiner et al. 2021). However, single-star evolutionary channels are also possible for Be stars (Hastings, Wang & Langer 2020) and so we cannot normally determine the evolutionary history in an individual case. In contrast, with an evolved star like θ Sco, the single-star evolutionary route is inconsistent with models and can be ruled out, leaving the binary route as the most likely option.

While our preferred model for the binary interaction does not involve the wider companion θ Sco B, we cannot exclude other scenarios in which this companion was involved. Further observations to spectroscopically characterize θ Sco B and better determine the orbit should help to clarify its involvement. If θ Sco B was not involved in the interaction then it should be a fairly normal main-sequence A star. If θ Sco B was responsible for transferring mass and angular momentum on to θ Sco A then it must have been initially the more massive star in the system, and would now be a stripped star. The kinematics of θ Sco show that it is not a runaway star, ruling out any interaction that involved ejection of components from the system.

We can expect to find other cases of evolved stars that are the result of binary evolution. The results presented here show that polarimetry is a useful tool for the detection and characterization of rapid rotation. Determining how common such objects are could have implications for testing predictions of binary evolution (Sana et al. 2012) and the importance of binary interactions for stellar-population synthesis models (e.g. Eldridge & Stanway 2009; Eldridge et al. 2017).

7 SUMMARY AND CONCLUSIONS

Multiwavelength, high-precision linear polarimetry of θ Sco has revealed a significant rotationally induced stellar-polarization signal arising in the A component. The rotational polarization in this evolved star is several times higher than that previously seen in rapidly rotating main-sequence stars (Cotton et al. 2017a; Bailey et al. 2020b) as expected due to the lower gravity.

A reanalysis of *Hipparcos* data provides the first reliable characterization of the visual-binary B component. We find that the B component is at sub-arcsecond separation (0.538 arcsec in 1991 and 0.245 arcsec in 2021), and is ∼3.3 mag fainter than component A. The polarimetry, combined with additional observational constraints, permits the determination of the rotation rate and other fundamental stellar parameters of θ Sco A at a level of precision not otherwise normally possible for single stars.

The rapid rotation we determine for θ Sco A ($\omega \geq 0.94$) is inconsistent with evolutionary models for single rotating stars (Georgy et al. 2013), which predict much slower rotation at this evolutionary stage. The mass we determine for θ Sco A is lower than that predicted by these models. We therefore conclude that θ Sco A is the result of a different evolutionary path, most likely interaction and eventual merger with a close binary companion.

Polarimetry can potentially be used to identify and characterize other rapidly rotating evolved stars and help to further investigate the role of binary interaction in stellar evolution.

ACKNOWLEDGEMENTS

DATA AVAILABILITY

The new polarization data used for this project are provided in Tables 2 and 3 of the paper.

REFERENCES

Ayres T. R., 2018, ApJ, 854, 95
Baade D. et al., 2016, A&A, 588, A56
Bailey J., Lucas P. W., Hough J. H., 2010, MNRAS, 405, 2570
Bailey J., Kedziora-Chudczer L., Cotton D. V., Bott K., Hough J. H., Lucas P. W., 2015, MNRAS, 449, 3064
Bailey J., Cotton D. V., Kedziora-Chudczer L., De Horta A., Maybour D., 2019, Nat. Astron., 3, 636
Bailey J., Cotton D. V., Kedziora-Chudczer L., De Horta A., Maybour D., 2020a, Publ. Astron. Soc. Aust., 37, e004
Bailey J., Cotton D. V., Howarth I. D., Lewis F., Kedziora-Chudczer L., 2020b, MNRAS, 494, 2254
Bailey J. et al., 2021, MNRAS, 502, 2331
Balona L. A., Ozuyar D., 2020, MNRAS, 493, 2528
Bessell M. S., 2000, PASP, 112, 961
Bodensteiner J. et al., 2021, in MOBSTER-1 virtual conference: Stellar Variability as a Probe of Magnetic Fields in Massive Stars. Zenodo, p. 24
Chandrasekhar S., 1946, ApJ, 103, 351
Code A. D., 1950, ApJ, 112, 22
Collins G. W., 1970, ApJ, 159, 583
Collins G. W., Truax R. J., Cranmer S. R., 1991, ApJS, 77, 541
Cotton D. V., Bailey J., Kedziora-Chudczer L., Bott K., Lucas P. W., Hough J. H., Marshall J. P., 2016, MNRAS, 455, 1607
Cotton D. V., Bailey J., Howarth I. D., Bott K., Kedziora-Chudczer L., Lucas P. W., Hough J. H., 2017a, Nat. Astron., 1, 690
Cotton D. V., Marshall J. P., Bailey J., Kedziora-Chudczer L., Bott K., Marsden S. C., Carter B. D., 2017b, MNRAS, 467, 873
Cotton D. V. et al., 2019, MNRAS, 483, 3636
Cotton D. V., Bailey J., Kedziora-Chudczer L., De Horta A., 2020, MNRAS, 497, 2175
Cotton D. V. et al., 2022, Nat. Astron., 6, 154
Davis L., Greenstein J. L., 1951, ApJ, 206
de Mink S. E., Langer N., Izzard R. G., Sana H., de Koter A., 2013, ApJ, 764, 166
Domiciano de Souza A., Bouchaud K., Rieutord M., Espinosa Lara F., Putigny B., 2018, A&A, 619, A167
Ducati J. R., Bevilacqua C. M., Rembold S. B., Ribeiro D., 2001, ApJ, 558, 309
Duchêne G., Kraus A., 2013, ARA&A, 51, 269
Eggenberger P., Meynet G., Maeder A., Hirschi R., Charbonnel C., Talon S., Ekström S., 2008, Ap&SS, 316, 43
Eldridge J. J., Stanway E. R., 2009, MNRAS, 400, 1019
Eldridge J. J., Stanway E. R., Xiao L., McClelland L. A. S., Taylor G., Ng M., Greis S. M. L., Bray J. C., 2017, Publ. Astron. Soc. Aust., 34, e058
Espinosa Lara F., Rieutord M., 2011, A&A, 533, A43
Frisch P. C. et al., 2010, ApJ, 724, 1473
Georgy C., Ekström S., Granada A., Meynet G., Mowlavi N., Eggenberger P., Maeder A., 2013, A&A, 553, A24
Gray R. O., Corbally Christopher J., 2009, Stellar Spectral Classification. Princeton Univ. Press, Princeton, NJ
Gray R. O., Garrison R. F., 1989, ApJS, 69, 301

Harrington J. P., Collins G. W., 1968, ApJ, 151, 1051

Hastings B., Wang C., Langer N., 2020, A&A, 633, A165

Howarth I. D., 2011, MNRAS, 413, 1515

Hubeny I., 2012, in Richards M. T., Hubeny I., eds, Proc. IAU Symp. 282, From Interacting Binaries to Exoplanets: Essential Modeling Tools, Cambridge Univ. Press, Cambridge. p. 221

Hubeny I., Stefl S., Harmanec P., 1985, Bull. Astron. Inst. Czech., 36, 214

Innes R. T. A., 1927, Southern Double Star Catalogue −19 deg. to −90 deg. Union Observatory, Johannesburg

Johnson H. L., Mitchell R. I., Iriarte B., Wisniewski W. Z., 1966, Commun. Lunar Planet. Lab., 4, 99

Jones E., Oliphant T., Peterson P. 2001, SciPy: Open Source Scientific Tools for Python, http://www.scipy.org/

Jones C. E. et al., 2021, preprint (arXiv:2111.07926)

Kerr M., Frew D., Jaworski R., 2006, The Deep-Sky Observer (the Quarterly Journal of the Webb Society), 141, 8

Kramers H. A., 1923, London Edinburgh Dublin Phil. Mag. J. Sci., 46, 836

Kurucz R. L., Bell B., 1999, CD-ROM No. 23: Atomic Line Data, available at http://kurucz.harvard.edu/cdroms.html

Marshall J. P. et al., 2016, ApJ, 825, 124

Marshall J. P., Cotton D. V., Scicluna P., Bailey J., Kedziora-Chudczer L., Bott K., 2020, MNRAS, 499, 5915

Piirola V. et al., 2020, A&A, 635, A46

Pols O. R., Cote J., Waters L. B. F. M., Heise J., 1991, A&A, 241, 419

Press W. H., Teukolsky S. A., Vetterling W. T., Flannery B. P., 2007, Numerical Recipes 3rd Edition: The Art of Scientific Computing, Cambridge Univ. Press, New York

Ricker G. R. et al., 2015, J. Astron. Telesc. Instrum. Syst., 1, 014003

Samus' N. N., Kazarovets E. V., Durlevich O. V., Kireeva N. N., Pastukhova E. N., 2017, Astron. Rep., 61, 80

Sana H. et al., 2012, Science, 337, 444

Scowen P. A. et al., 2021, in Barlo A. A., Breckinbridge, J. B., Stahl, H. P.eds, Proc. SPIE Conf. Ser. Vol. 11819, UV/Optical/IR Space Telescopes and Instruments: Innovative Technoloies and Concepts X. SPIE, Bellingham, p. 1181908

Seaton M. J., 1979, MNRAS, 187, 73

See T. J. J., 1896, Astron. Nachr., 142, 43

Serkowski K., 1971, in IAU Colloq. 15: New Directions and New Frontiers in Variable Star Research. Cambridge Uinv. Press, Cambridge, p. 11

Serkowski K., 1973, in Greenberg J. M., van de Hulst H. C., eds, Proc. IAU Symp. 52, Interstellar Dust and Related Topics. D. Reidel, Dordrecht, p. 145

Serkowski K., Mathewson D. S., Ford V. L., 1975, ApJ, 196, 261

Sonneborn G., 1982, in Jaschek M., Groth H. G., eds, Proc. IAU Symp. 98, Be Stars. D. Reidel., Dordrecht, p. 493

Spurr R. J. D., 2006, J. Quant. Spectrosc. Radiat. Transfer, 102, 316

Tokovinin A., 2018, PASP, 130, 035002

Tokovinin A., Mason B. D., Mendez R. A., Costa E., Mann A. W., Henry T. J., 2021, AJ, 162, 41

van Belle G. T., 2012, A&AR, 20, 51

van Leeuwen F., 2007, Astrophysics and Space Science Library, Vol. 350, *Hipparcos*, the New Reduction of the Raw Data. Springer-Verlag, Berlin

Whittet D. C. B., Martin P. G., Hough J. H., Rouse M. F., Bailey J. A., Axon D. J., 1992, ApJ, 386, 562

Wilking B. A., Lebofsky M. J., Martin P. G., Rieke G. H., Kemp J. C., 1980, ApJ, 235, 905

This paper has been typeset from a TEX/LATEX file prepared by the author.